RSC Advances

PAPER

View Article Online
View Journal | View Issue

Cite this: *RSC Adv.*, 2026, **16**, 1697

Engineering of a kaolin/SLS-functionalized biochar@β-cyclodextrin composite for adsorption of *o*-nitrophenol; optimization, mechanistic study, and Box–Behnken design

Abdelazeem S. Eltaweil, [ab] Nouf Al Harby, *[c] Mervette El Batouti [b] and Eman M. Abd El-Monaem [d]

In this investigation, a good adsorbent was created by combining kaolin, β-cyclodextrin, and sodium lauryl sulfate-functionalized biochar, resulting in a new Kaol/SLS-BC/β-CD composite. Assorted analyses were used to characterize the chemical/physical properties of the Kaol/SLS-BC/β-CD. The adsorption capability of the Kaol/SLS-BC/β-CD was evaluated, using an experimental adsorption batch study of *o*-nitrophenol (*o*-NP). The experimental batch experiments showed that *o*-NP removal of 100% was achieved at room temperature after 180 minutes with pH = 3, Kaol/SLS-BC/β-CD dose = 10 mg, and *o*-NP concentration = 50 mg L^{-1}. Kinetic and isotherm analyses of the experimental data implied that the Freundlich isotherm model and the pseudo-second-order kinetic model were obeyed for the *o*-NP adsorption reaction. Surprisingly, the maximal adsorption capacity of Kaol/SLS-BC/β-CD towards *o*-NP, calculated from Langmuir analysis, was 588.24 mg g^{-1}. The optimization of *o*-NP adsorption onto Kaol/SLS-BC/β-CD was investigated using response surface methodology (RSM) based on a Box–Behnken design (BBD) with three independent variables: initial *o*-NP concentration, adsorbent dosage, and contact time. The quadratic response surface model was validated through analysis of variance (ANOVA). The reduced quadratic model demonstrated good agreement between the predicted and experimental results. Thus, the validated model can be reliably applied to predict the optimal conditions for *o*-NP adsorption onto Kaol/SLS-BC/β-CD. The mechanistic study of the *o*-NP adsorption onto Kaol/SLS-BC/β-CD clarified that the process may occur *via* Lewis acid–base, pore-filling, coordination bond, hydrogen bond, and pi–pi interactions. Notably, the cycling test indicated that the Kaol/SLS-BC/β-CD could be reused for six adsorption cycles of *o*-NP with promising efficacy.

Received 19th October 2025
Accepted 26th November 2025

DOI: 10.1039/d5ra08005c

rsc.li/rsc-advances

1. Introduction

Water pollution is the worst environmental issue for the planet due to its fatal effects on humans, causing numerous diseases such as cholera, hepatitis, typhoid, liver damage, and cancer. Therefore, researchers have focused on reducing the amount of dangerous water pollutants that have resulted from the global expansion of industry and agriculture, and worldwide population growth.[1] Mineral acids, heavy metals, pharmaceuticals, artificial dyes, and aromatic compounds are examples of accumulated contaminants in water bodies.[2,3] *o*-Nitrophenol (*o*-NP) is a primary substance used in large-scale industries, such as producing insecticides, pigments, fungicides, pharmaceuticals, herbicides, chemical intermediates, petrochemicals, and explosives. As a consequence, *o*-NP is produced in high quantities, ranging from ten to fifteen million pounds annually.[4]

The high production and excessive usage of *o*-NP result in it being discharged into water bodies, leading to harmful impacts on human health, including drowsiness, cyanosis, blurred vision, mouth irritation, and damage to the kidneys and liver.[5–7] For this reason, many remediation techniques have been tested and developed to increase their potential to remove *o*-NP from wastewater, including electrolysis, Fenton degradation, membrane filtration, adsorption, and coagulation.[8,9] Our study highlights the use of an adsorption process because of its cost-effectiveness, eco-friendliness, simple processing, and high reusability, aiming to identify an effective adsorbent with excellent adsorption capacity and recyclability for *o*-NP.[10]

Clays are deemed superior adsorbents due to their high surface area, antimicrobial activity, low price, non-toxicity, small particle size, high availability, stable structure,

[a]*Department of Engineering, College of Engineering and Technology, University of Technology and Applied Sciences, Ibra, Sultanate of Oman*

[b]*Department of Chemistry, Faculty of Science, Alexandria University, Alexandria, 21934, Egypt*

[c]*Department of Chemistry, College of Science, Qassim University, Buraidah 51452, Saudi Arabia. E-mail: hrbien@qu.edu.sa*

[d]*Advanced Technology Innovation, Borg El-Arab, Alexandria, Egypt*

biocompatibility, and cation exchange capability. Because of the plentiful oxygenated functional groups in clay structures, they can interact with large amounts of pollutants through physical and chemical mechanisms, such as hydrophobic interactions, ion exchange, electrostatic interactions, and surface complexation.[11,12] Kaolin is an important phyllosilicate clay with a sheet-like structure constructed by the bonding tetrahedral Si–O and octahedral Al–O sheets with hydrogen bonds. The empirical formula of kaolin is $Al_4Si_4O_{10}(OH)_8$, and its crystallite structure comprises tetrahedral Si–O in the silica face and Al–OH in the alumina face, while the crystal's edges contain Si–OH and Al–OH. Upon counting the net charge of kaolin, it was found that it equals zero ($[4 \times 4] + [4 \times 3] + [10 \times -2] + [8 \times -1] = 0$); however, kaolin carries a low negative charge owing to the broken edges of the kaolin crystal.[13] This negative charge occurs only on the surface of kaolin, while the inner crystal remains uncharged. Notably, the branched hydroxyl groups on the kaolin crystal's edges are the governing reactive sites that contribute to the adsorption process.[14] Nevertheless, previous studies regarding the application of kaolin as a green adsorbent demonstrate its inferior adsorption capability. Therefore, numerous investigations have involved studying various modification techniques for improving adsorption by kaolin, comprising milling, chemical treatments, heat treatments, and mechanochemical activation.[15]

Biochar is a porous carbonaceous material fabricated by pyrolyzing organic biomass in an oxygen-free environment.[16] Different feedstocks, such as algae, forestry waste, agriculture waste, poultry manure, and domestic garbage, are applied for fabricating biochar.[17,18] Biochar has achieved exceptional fame among diverse adsorbent types due to its porous structure, copious oxygen-containing functional groups, unique mechanical strength, economic-environmental merits, excellent adsorption ability, and high surface area.[19] Some studies have demonstrated the significant role of surfactant functionality in enhancing the adsorption by biochar, as surfactants enrich the surface charge of biochar and improve its hydrophobicity. Notably, different types of surfactants revealed exceptional improvement in the adsorption capacity of biochar, including gemini surfactants, cationic, nonionic, anionic surfactants, and a combination of double surfactants.

Cyclodextrins are cyclic oligosaccharides composed of connected glucopyranose rings in a cone shape.[20] Cyclodextrins classified into three types: α-, β-, and γ-cyclodextrin with different cavity sizes and glucopyranose ring numbers.[21–23] β-cyclodextrin is a preferred form compared to the other analogs because of its easy preparation and appropriate cavity size (0.6–0.65 nm).[24] Cyclodextrins consist of the hydrophobic CH_2 and the hydrophilic OH, forming a host–guest architecture.[25] Cyclodextrins are distinguished by their biocompatibility, porous structure, large surface area, sustainable production, and facile functionalization.[26–28] Interestingly, the abundant hydroxyl species on the surface of cyclodextrin endow it with a high capability to chelate pollutants from wastewater, rendering it an efficient adsorbent.[29]

In this context, our study highlights an excellent adsorbent to remove *o*-NP from wastewater. A new composite was prepared from kaolin, sodium lauryl sulfate-functionalized biochar, and β-cyclodextrin, forming a Kaol/SLS-BC/β-CD composite. Then, the chemical and physical properties of Kaol/SLS-BC/β-CD were studied using different characterization analyses. The optimization of the *o*-NP adsorption process onto Kaol/SLS-BC/β-CD was investigated using batch experiments and theoretically by Box–Behnken design (BBD). The nature of interactions between Kaol/SLS-BC/β-CD and *o*-NP was deduced by analyzing the experimental data by kinetic and isotherm models. In addition, XPS spectroscopy was used to analyze the used and pure Kaol/SLS-BC/β-CD and determine the adsorption interactions between the composite and the *o*-NP molecules. The recyclability of Kaol/SLS-BC/β-CD was evaluated in light of the cycling test results for six adsorption runs of *o*-NP.

2. Experimental

2.1. Chemical substances

Sodium lauryl sulfate and kaolin were supplied by Aladdin Reagent Co., Ltd. β-cyclodextrin was bought from Rankem, and *o*-nitrophenol was provided by Merck.

2.2. Preparation of SLS-BC

First, the BC was derived by the thermochemical decomposition method from green algae collected from the Alexandria coastal area (Egypt). The green algae were rinsed repeatedly with tap water and distilled water to remove dust and impurities. The green algae were kept for a day in an oven at 60 °C and then smashed to a fine powder using a mortar and pestle. The green algae powder was calcined for 3 hours in a muffle at 500 °C, forming a jet-black solid of BC. Second, the BC powder was functionalized by SLS as follows: 0.36 g of SLS was mixed with 1.0 g of BC in 25 mL of distilled water for 45 minutes. The obtained SLS-functionalized BC remained for 2 hours in an oven at 100 °C for solvent evaporation. The dried SLS-functionalized BC was washed with distilled water to eliminate the SLS residues and then dried at 100 °C for 12 hours.

2.3. Preparation of Kaol/SLS-BC/β-CD

The Kaol/SLS-BC/β-CD composite was fabricated simply by the physical post-synthetic approach. In separate containers, different mass ratios of Kaol, SLS-BC, and β-CD were mixed in 20 mL of distilled water. They sonicated in a water bath an hour. The suspended solid of Kaol/SLS-BC/β-CD was collected using centrifugation and dried at 60 °C in an oven for 10 hours. Kaol/SLS-BC/β-CD was labeled as Kaol/SLS-$BC_{0.5}$/β-$CD_{0.5}$, $Kaol_{0.5}$/SLS-$BC_{0.5}$/β-CD, and $Kaol_{0.5}$/SLS-BC/β-$CD_{0.5}$ for mass ratios of Kaol, SLS-BC, and β-CD of 2 : 1 : 1, 1 : 1 : 2, and 1 : 2 : 1.

2.4. Characterization analyses

The Kaol/SLS-BC/β-CD composite was analyzed using a number of characterization techniques, including X-ray diffraction (PANalytical – XRD), to study the crystalline nature of the composite and the pure Kaol, SLS-BC, and β-CD. Furthermore, the compositions of Kaol, SLS-BC, β-CD, and Kaol/SLS-BC/β-CD were investigated by Fourier transform infrared spectroscopy

Table 1 Level and code of variables for the Box–Behnken design for *o*-NP adsorption onto Kaol/SLS-BC/β-CD

			Coded levels		
Coded variables	Actual variables	Unit	Low (−1)	Center (0)	High (+1)
A	Initial *o*-NP concentration	mg L^{-1}	50	175	300
B	Adsorbent dosage	mg	5	10	15
C	Contact time	min	2	61	120

(Frontier, PerkinElmer – FTIR). The outer morphologies of Kaol, SLS-BC, β-CD, and Kaol/SLS-BC/β-CD were determined using a scanning electron microscope (JEOL 7500F – SEM). Moreover, the surface charge of Kaol/SLS-BC/β-CD was determined at varied pHs by zeta potential measurements (Malvern – ZP). The elemental compositions of the fresh and used Kaol/SLS-BC/β-CD composites were defined using an ESCALAB 250XI (XPS).

2.5. Batch experiments

To establish the adsorption of the *o*-NP–Kaol/SLS-BC/β-CD system, optimal adsorption conditions were examined through various batch experiments. A comparison test was performed between the capabilities of the Kaol/SLS-BC/β-CD composites to adsorb *o*-NP. The pH influence on the *o*-NP adsorption ability was studied by varying the pH of the adsorption medium from 3 to 5, 7, 9, and 11. The economically favorable dosage of Kaol/SLS-BC/β-CD was identified after testing the removal percentages of *o*-NP by 5, 7, 10, and 15 mg of the composite. The temperature effects on the adsorption ability in the *o*-NP–Kaol/SLS-BC/β-CD system were deduced by changing the temperature from 20 °C to 30, 40, and 50 °C. The impact of the *o*-NP concentration was defined by increasing it from 50 to 100, 200, and 300 mg L^{-1} at a constant Kaol/SLS-BC/β-CD dose. Notably, all the adsorption experiments were performed in triplicate to validate the results. By measuring the initial (C_i) and final (C_f) *o*-NP concentrations using a spectrophotometer at a wavelength of 344 nm, the removal % and the adsorption efficiency of *o*-NP were identified using eqn (1) and (2):

$$R(\%) = \frac{C_i - C_f}{C_i} \times 100 \quad (1)$$

$$q(\text{mg g}^{-1}) = \frac{(C_i - C_f) \times V}{m} \quad (2)$$

2.6. Recyclability test

To examine the reusability potential of Kaol/SLS-BC/β-CD, the used composite was recollected after the *o*-NP adsorption and soaked in NaOH (20 mL, 1 M) under gentle stirring to get rid of all adsorbed *o*-NP. Then, the recycled Kaol/SLS-BC/β-CD was washed repeatedly with distilled H_2O and reused in the subsequent cycle.

2.7. Experimental setup for response surface methodology

Consistent with earlier reports,[30–32] three independent variables were selected for the study: the initial *o*-NP concentration (*A*), the adsorbent dosage (*B*), and the contact time (*C*). Each variable was evaluated at three levels (coded as −1, 0, and +1), as detailed in Table 1. The statistical analysis was performed using Design-Expert 13 software, which enabled both regression modeling and graphical interpretation of the experimental data for *o*-NP adsorption onto Kaol/SLS-BC/β-CD. The experimental plan was optimized using a Box–Behnken design (BBD), comprising 15 runs. To minimize potential errors from uncontrolled factors, the run order was randomized. The center point was repeated three times to allow for the estimation of experimental error and curvature. The design matrix and corresponding results, presented in Table 1, used conditions previously identified as optimal for *o*-NP adsorption. A second-order polynomial model was employed within the BBD framework to establish the regression equation describing the adsorption process of *o*-NP onto Kaol/SLS-BC/β-CD.

To determine the optimum adsorption conditions, a polynomial function incorporating quadratic terms is required. Typically, a second-order polynomial equation is employed (eqn (3)):

$$Y = b_0 + \sum_{i=1}^{k} b_i x_i + \sum_{i \le i \le j}^{k} b_{ij} x_i x_j + \sum_{i=1}^{k} b_{ii} {x_i}^2 \quad (3)$$

where *Y* represents the predicted response, x_k denotes the coded values of the independent variables, *k* is the number of variables considered, b_0 is the intercept, b_i is the linear coefficient, b_{ij} is the interaction coefficient, and b_{ii} is the quadratic coefficient.

The experimental data are utilized to estimate the model coefficients, and the coefficient of determination is then calculated to evaluate the adequacy of the regression model in describing the experimental results. Fisher's analysis of variance (ANOVA) is applied to assess the significance of individual coefficients. When a regression coefficient b_i differs significantly from zero, the corresponding independent variable x_i is considered to exert a significant effect on the response.

3. Results and discussion

3.1. Investigating the characteristics of Kaol/SLS-$BC_{0.5}$/β-$CD_{0.5}$

3.1.1. Chemical structure. The chemical structures of the synthesized Kaol, BC, SLS-BC, β-CD, and Kaol/SLS-$BC_{0.5}$/β-$CD_{0.5}$ composite were investigated, according to the FTIR spectra (Fig. (1a)). For the Kaol spectrum, the outer Al–OH stretching peaks were observed at 3657 and 3695 cm^{-1}, and the stretching peak of the inner Al–OH appeared at 3623 cm^{-1}.[33] The absorption peaks at 694, 755, and 791 cm^{-1} are ascribed to stretching

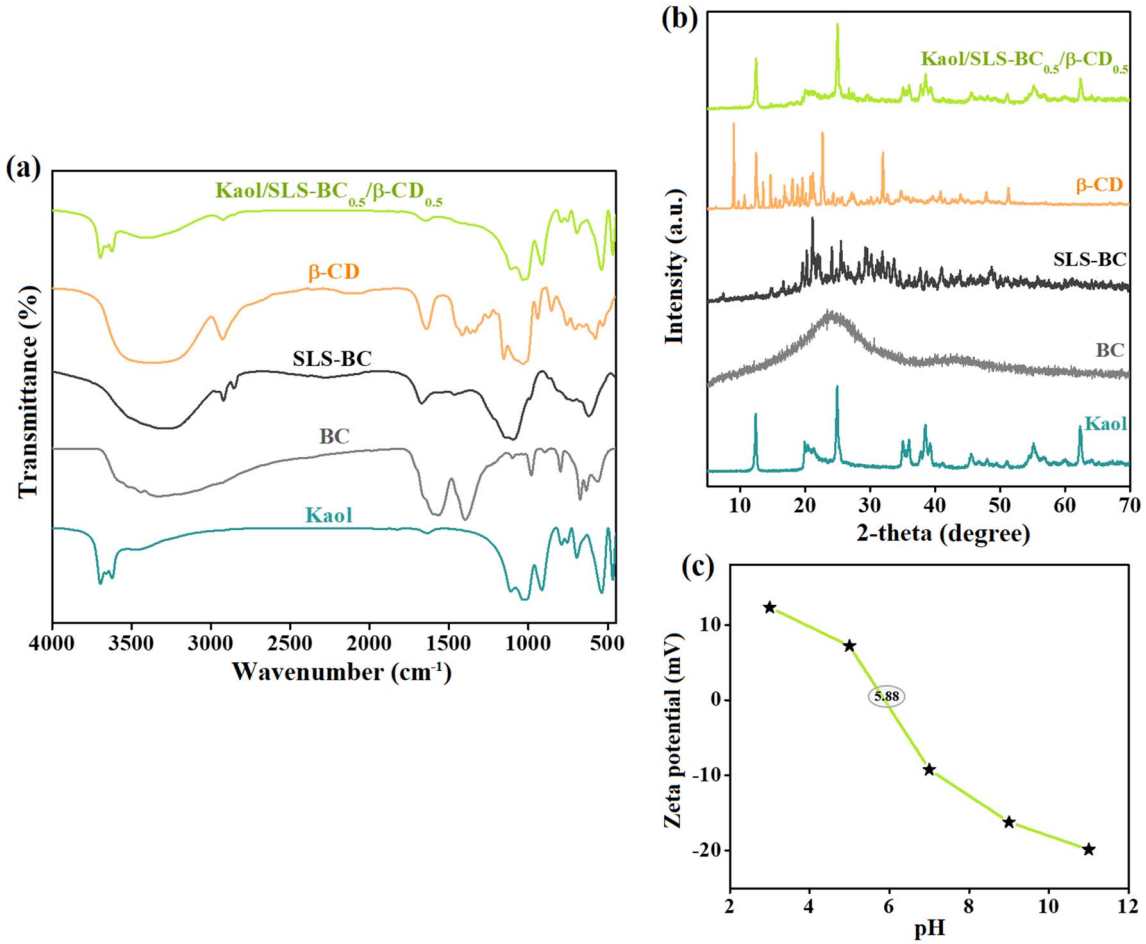

Fig. 1 (a) FTIR spectra and (b) XRD spectra of Kaol, BC, SLS-BC, β-CD, and Kaol/SLS-$BC_{0.5}$/β-$CD_{0.5}$, and (c) ZP curve of Kaol/SLS-$BC_{0.5}$/β-$CD_{0.5}$.

of the Si–O group, and the corresponding peaks for Si–O–Si emerged at 1034 and 1110 cm^{-1}.[34] The Al–OH peak was present at 915 cm^{-1}, while the absorption peaks at 535 and 469 cm^{-1} are assigned to Si–O–Al.[35] For the BC spectrum, the absorption peaks at 1089 and 1487 cm^{-1} are attributed to C–O and O–C=O. The related peaks of the C–H, Si–O, and C=O functional groups of the BC were observed at 797, 458, and 1509 cm^{-1}, respectively.[36] For the SLS-BC spectrum, there is an obvious decrease in the intensity of the pure BC peaks after SLS functionalization, reflecting the occurrence of chemical interactions between BC and SLS. Furthermore, new absorption peaks were revealed at 2921 and 2961 cm^{-1}, which correspond to asymmetric and symmetric C–H vibration of CH_2 of SLS. In addition, the peaks at 1095 and 1466 cm^{-1} are accompanied by symmetric and asymmetric S=O vibration.[37] These FTIR observations suggested the good functionality of SLS on the BC surface. For the β-CD spectrum, vibrating and stretching C–O peaks emerged at 1152 and 1252 cm^{-1}. The absorption peaks at 1643 cm^{-1} belong to the bending vibration of O–H, while the stretching vibration of O–H appeared at 3362 cm^{-1}. The stretching C–H bond was shown at 2925 cm^{-1}, while the absorption peaks of the bending C–H bond were observed at 766, 1365, 1414, and 1365 cm^{-1}. For the Kaol/SLS-$BC_{0.5}$/β-$CD_{0.5}$ spectrum, the accompanying peaks for Kaol, SLS-BC, and β-CD emerged, indicating the successful integration of the components. In addition, the peaks related to Kaol were revealed with higher clarity because of its higher dose in the composite's matrix.

3.1.2. Crystallographic character. The crystallographic properties of Kaol, BC, SLS-BC, β-CD, and the Kaol/SLS-$BC_{0.5}$/β-$CD_{0.5}$ composite were studied using XRD spectra, as shown in Fig. (1b). For the Kaol spectrum, the distinguishing diffraction peaks of Kaol emerged at 2θ of 12.41°, 19.96°, 21.37°, 24.92°, 35.96°, 37.78°, 38.48°, 39.20°, 45.54°, 47.90°, 49.52°, 51.05°, and 62.31°.[38] For the BC spectrum, a wide characteristic diffraction peak was revealed at 2θ of 25°.[39] For the SLS-BC spectrum, new related diffraction peaks related to SLS were revealed at 2θ of 20.24°, 21.96°, 24.08°, 25.50°, 29.49°, 30.18°, 34.57°, 43.79°, 45.93°, 48.40°, and 50.01°.[40] For the β-CD spectrum, the peaks corresponding to β-CD emerged at 2θ of 6.29°, 8.8°, 9.76°, 10.69°, 11.69°, 12.47°, 14.70°, 17.15°, 21.19°, 22.69°, 24.34°, 27.14°, 35.9°, and 41.47°.[41–43] For the Kaol/SLS-$BC_{0.5}$/β-$CD_{0.5}$ spectrum, the diffraction peaks of Kaol are dominant in the spectrum, with its mass in the composite double both those of SLS-BC and β-CD. Furthermore, the intensity of Kaol peaks in the composite is higher than in the pure Kaol, confirming its interaction with SLS-BC and β-CD.

3.1.3. Surface charge. The net charges on the Kaol/SLS-$BC_{0.5}$/β-$CD_{0.5}$ composite at various pHs were determined by ZP, as illustrated in Fig. (1c). The ZP *vs.* pH curve showed that the point of zero-charge of Kaol/SLS-$BC_{0.5}$/β-$CD_{0.5}$ was at pH = 5.88, meaning that the composite's surface is positively charged at pH values below 5.88 and negatively charged above it. Furthermore, the ZP values of Kaol/SLS-$BC_{0.5}$/β-$CD_{0.5}$ at pHs 3, 5, 7, 9, and 11 were 12.33, 7.22, −9.23, −16.22, and −19.89 mV, respectively. These observations indicated the suitability of Kaol/SLS-$BC_{0.5}$/β-$CD_{0.5}$ for adsorbing anionic and cationic contaminants.

3.1.4. Study of SLS loading on BC. Fig. S1 shows the EDX spectra of pristine BC and the as-fabricated SLS-BC before and after washing. Notably, the EDX spectrum of SLS-BC showed clear signals of Na and S with atomic percentages of 0.89 and 3.72%, confirming the successful SLS functionality on the BC surface. Furthermore, the carbon atomic % after SLS functionalization increased from 66.71 to 73.35%, while the oxygen atomic % decreased from 33.03 to 22.01% because of surface coverage by the SLS alkyl chains. The EDX spectrum of SLS-BC after washing showed the disappearance of the sodium peak, with a decrease in the sulfur atomic % to 1.85%. This observation implied the removal of the loosely bound SLS molecules. Moreover, the increase in the oxygen atomic % in the purified SLS-BC sample to 26.50% is most likely due to re-exposure of the underlying oxygenated functional groups of biochar once excess SLS is removed. Accordingly, these results showed that only a small fraction of SLS remains strongly attached to the BC surface, while most of the loaded SLS is eliminated through washing.

3.1.5. Outer morphology. The outer morphologies of Kaol, β-CD, BC, SLS-BC, and the Kaol/SLS-$BC_{0.5}$/β-$CD_{0.5}$ composite were analyzed using an SEM microscope, as shown in Fig. (2a–e). The morphology of pure Kaol appears like smashed sheets with irregular sizes. The SEM of the neat β-CD reveals a layer-like shape stacked horizontally with perfect order. The morphology of the green algae-derived BC appeared as a corrugated sheet, forming wide vacancies, giving it flexibility for functionalization and doping. In addition, the outer morphology of BC enables it to act as a promising supporter for Kaol and β-CD. The SLS-BC image clarifies the spreading of the SLS particles on the BC surface, which further confirms the successful SLS functionalization of the BC surface. The SEM image of Kaol/SLS-$BC_{0.5}$/β-$CD_{0.5}$ shows the support of Kaol and β-CD on the SLS-BC surface.

3.1.6. Elemental composition. Fig. (3a–f) illustrate the XPS spectra of the Kaol/SLS-$BC_{0.5}$/β-$CD_{0.5}$ composite, revealing its elemental composition. The wide spectrum of Kaol/SLS-$BC_{0.5}$/β-$CD_{0.5}$ shows that it comprises silicon, aluminum, carbon, sulfur, and oxygen with atomic percentages of 13.15, 11.87, 19.45, 3.31, and 52.22%. For the sulfur spectrum, the peaks accompanying S^{2-}, SO_4^{2-}, and S–O of SLS appeared at 166.33, 168.04, and 168.51 eV, with atomic % of 5.27, 0.59, and 94.15%.[44] For the silicon spectrum, two broad peaks with high intensity emerged at 102.21 and 102.83 eV, which are attributed to Si^{2+} and SiO_2, with atomic percentages of 36.49 and 63.51%, respectively.[45] The aluminum spectrum revealed the peak corresponding to Al–O at a binding energy of 74.24 eV.[46] The peaks corresponding to Al–O and Si–O emerged in the oxygen spectrum with atomic % of 47.86 and 52.14% at binding energies of 531.64 and 532.08 eV. The carbon spectrum shows a peak corresponding to C–H and C–C at 284.41 eV with an atomic % of 49.99%. Furthermore, the observed peaks at 286.13 and 286.70 eV are ascribed to C–O/O–H (12.35%) and C═O (37.67%).

3.2. Identifying the best adsorption conditions for *o*-NP

3.2.1. Comparison test. Fig. (4a) shows the results from the comparison study between the removal efficiency of Kaol, BC, SLS-BC, β-CD, and Kaol/SLS-BC/β-CD composites toward *o*-NP. The removal percentages of *o*-NP by Kaol, BC, SLS-BC, β-CD, Kaol/SLS-$BC_{0.5}$/β-$CD_{0.5}$, $Kaol_{0.5}$/SLS-$BC_{0.5}$/β-CD, and $Kaol_{0.5}$/SLS-BC/β-$CD_{0.5}$ were recorded as 79.71, 52.47, 63.28, 60.08, 94.92, 58.42, and 63.75%, while their adsorption efficiencies were 78.94, 62.32, 70.89, 68.35, 94.18, 58.73, and 64.02 mg g^{-1}, respectively. These findings demonstrated the improvement of

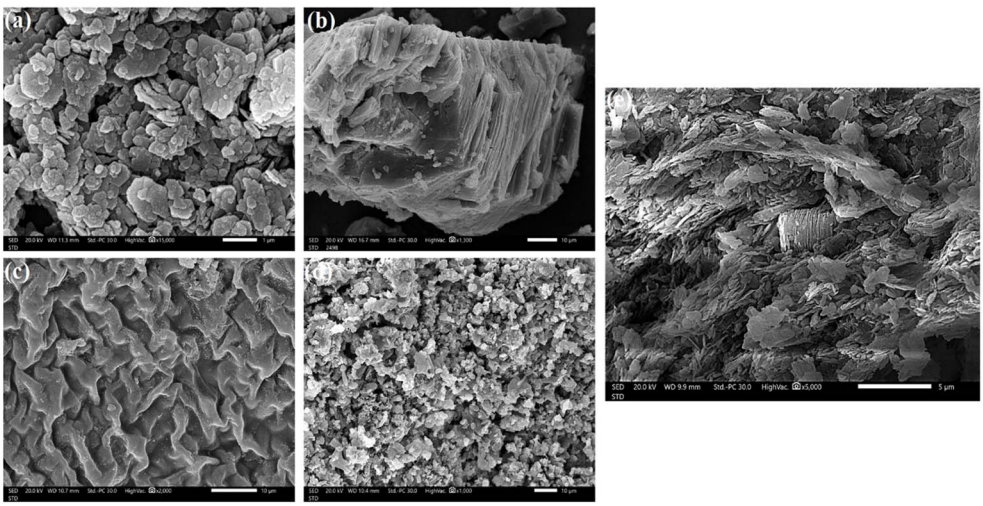

Fig. 2 SEM images of (a) Kaol, (b) β-CD, (c) BC, (d) SLS-BC, and (e) the Kaol/SLS-$BC_{0.5}$/β-$CD_{0.5}$ composite.

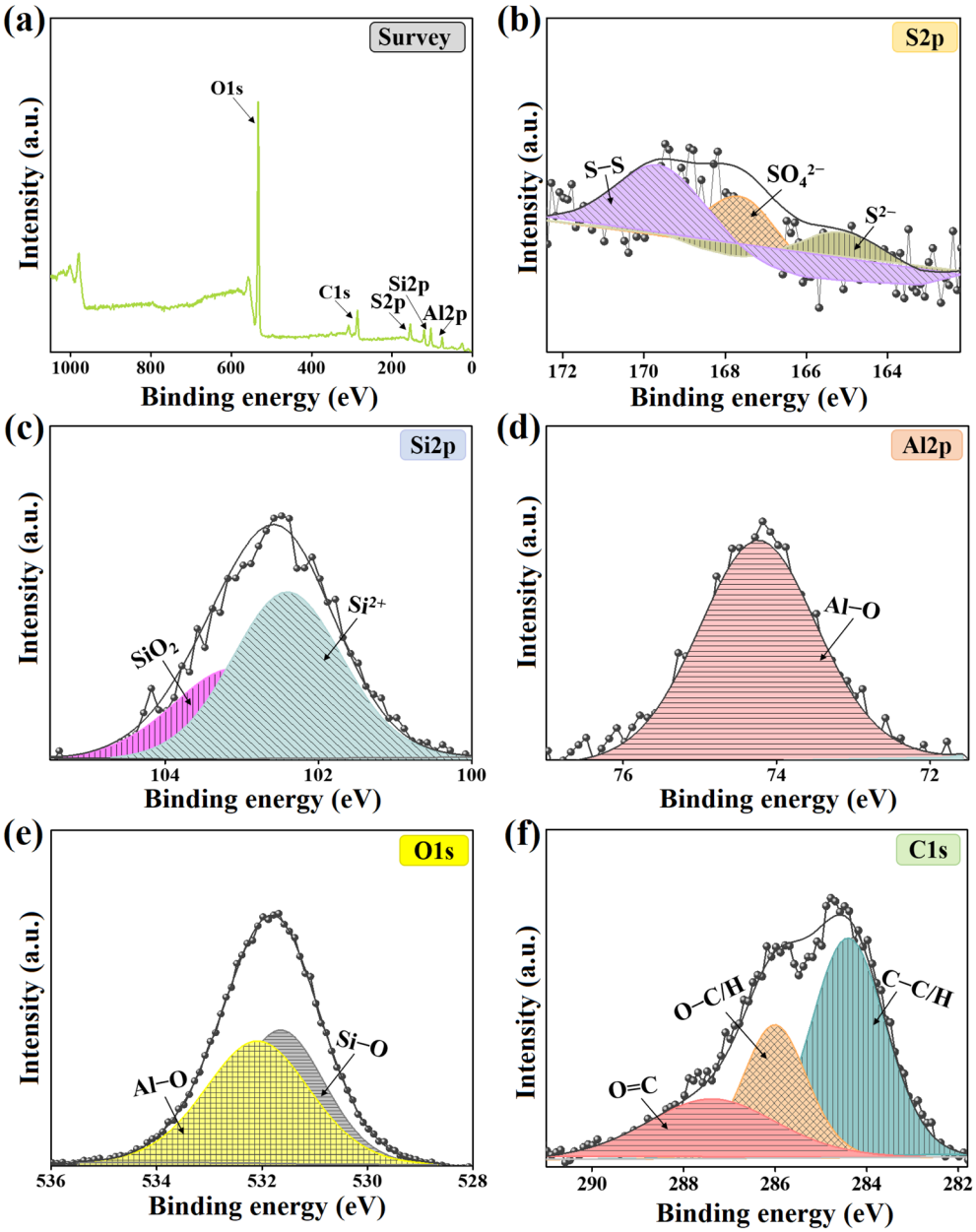

Fig. 3 XPS spectra of the Kaol/SLS-$BC_{0.5}$/β-$CD_{0.5}$ composite: (a) XPS survey, (b) S2p, (c) Si2p, (d) Al2p, (e) O1s, and (f) C1s.

the adsorption capacity of BC as a result of the positive influence of the SLS functionality, which provides BC with sulfate groups that act as a Lewis base, strengthening the Lewis acid–base interaction between SLS-BC and *o*-NP. Furthermore, mixing Kaol, SLS-BC, and β-CD resulted in a synergistic effect as the adsorption capacities of the three composites are higher than those of the pure materials. In addition, the best mass ratio of Kaol, SLS-BC, and β-CD was 2 : 1 : 1, so Kaol/SLS-$BC_{0.5}$/β-$CD_{0.5}$ was used in the rest of the batch adsorption experiments for *o*-NP.

3.2.2. Impact of the pH of the adsorption system. The pH of adsorption media significantly impacts the ionic state of the *o*-NP molecules, since they are still in their molecular form until the pH is increased to 7.23, at which point the *o*-NP molecules exist in anionic form .[47] Therefore, it is essential to discuss the effect of increasing the adsorption pH of the medium on the adsorption ability of the *o*-NP–Kaol/SLS-$BC_{0.5}$/β-$CD_{0.5}$ system. Fig. (4b) shows a decrease in the adsorption capacity of *o*-NP from 94.18 to 54.60 mg g^{-1} and removal % from 94.92 to 60.38%, sequentially. This adsorption performance can be anticipated by the generated electrostatic repulsion forces between the anionic *o*-NP molecules and the negative charges on the Kaol/SLS-$BC_{0.5}$/β-$CD_{0.5}$ surface.[48] Notably, electrostatic interaction is the dominant adsorption pathway in most of the adsorption processes; however, in the removal of nitrophenol derivatives, it has no domination in the adsorption mechanism. Meanwhile, pathways like Lewis acid–base, pore-filling,

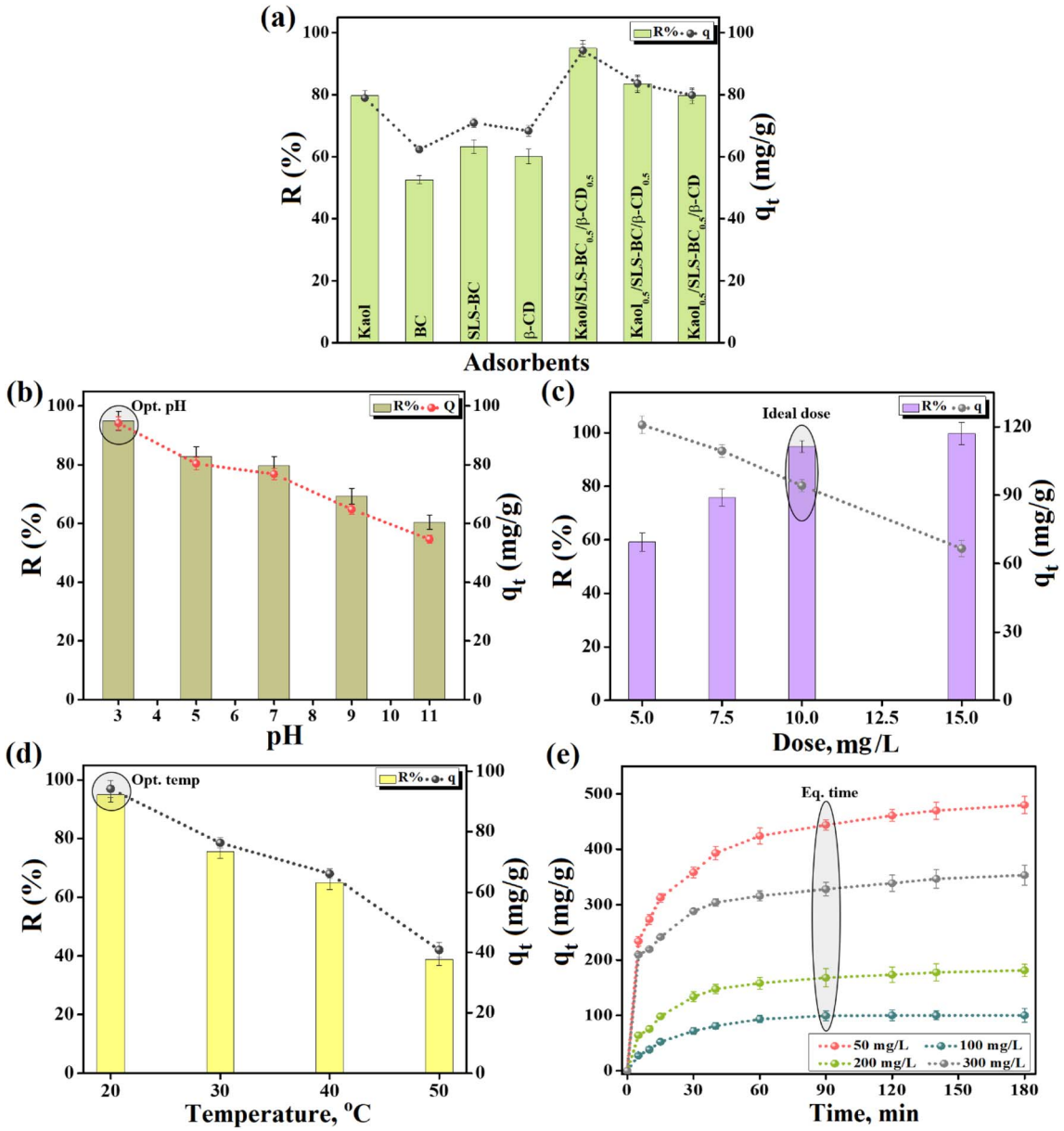

Fig. 4 The experimental results for the *o*-NP adsorption: (a) optimizing the mass ratio of the Kaol/SLS-BC/β-CD composite, (b) identifying the optimal pH of the medium, (c) determining a suitable Kaol/SLS-BC$_{0.5}$/β-CD$_{0.5}$ dose, (d) investigating the thermal behavior, and (e) studying the adsorption capability of the Kaol/SLS-BC$_{0.5}$/β-CD$_{0.5}$ composite towards different *o*-NP concentrations.

complexation, and hydrophobic interactions are responsible for the adsorption of the nitrophenol derivatives.

3.2.3. Impact of the Kaol/SLS-BC$_{0.5}$/β-CD$_{0.5}$ dosage. The weight of the used adsorbent in removing targeted contaminants with high efficiency is a key parameter. Therefore, the adsorptive removal of *o*-NP was evaluated using different dosages of Kaol/SLS-BC$_{0.5}$/β-CD$_{0.5}$, increasing from 5 to 15 mg. Fig. (4c) depicts an improvement in the removal % of *o*-NP from 59.08 to 99.78% and a decrease in its adsorption capacity from 120.85 to 66.52 mg g^{-1} with increasing Kaol/SLS-BC$_{0.5}$/β-CD$_{0.5}$ mass from 5 to 15 mg. The increase in the *o*-NP adsorption % with an increase in the Kaol/SLS-BC$_{0.5}$/β-CD$_{0.5}$ dosage can be explained by the greater availability of adsorption sites. The decrease in the adsorption capacity of *o*-NP is because of the resulting decrease in the available surface area owing to the aggregation of the excess amount of Kaol/SLS-BC$_{0.5}$/β-CD$_{0.5}$.

3.2.4. Impact of the processing temperature. Fig. (4d) shows the adsorption performance of Kaol/SLS-BC$_{0.5}$/β-CD$_{0.5}$ toward *o*-NP at various system temperatures. The experimental results showed the exothermic adsorption performance of the *o*-NP–Kaol/SLS-BC$_{0.5}$/β-CD$_{0.5}$ system, clarifying a decrease in the adsorption capacity of *o*-NP from 94.18 to 40.84 mg g^{-1} and the removal % from 94.92 to 38.84% when the processing temperature was increased from 20 to 50 °C. These findings can be attributed to faster *o*-NP Brownian motion inside the adsorption system, decreasing the number of *o*-NP molecules reaching the

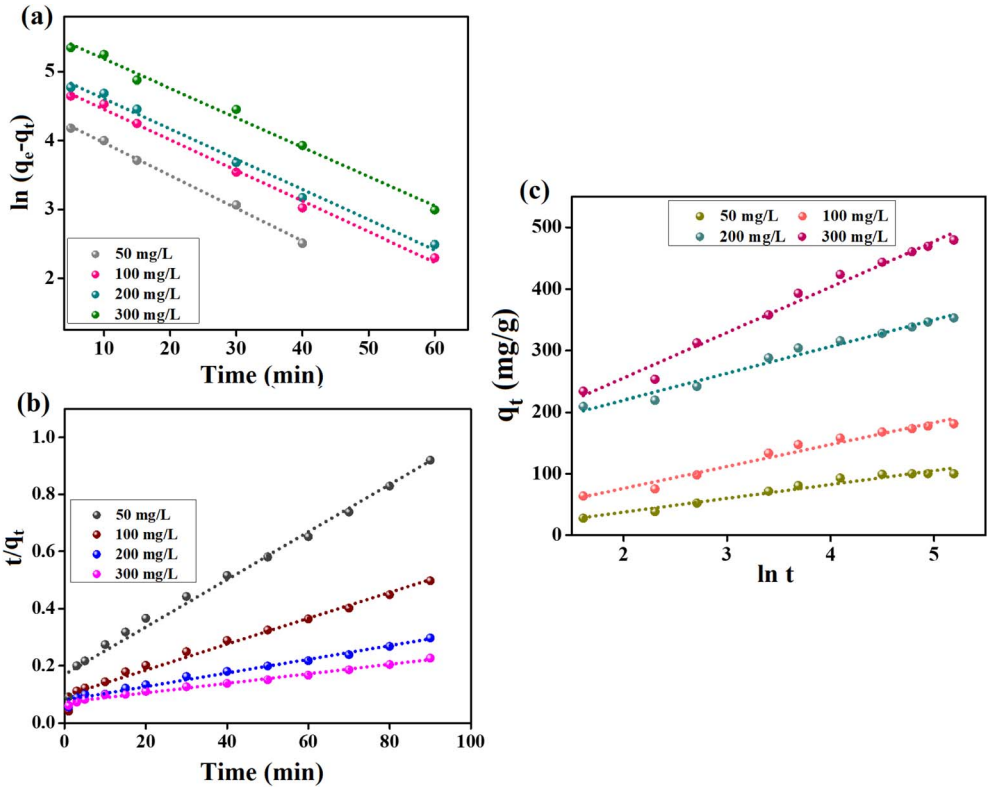

Fig. 5 Kinetic investigations of *o*-NP adsorption onto the Kaol/SLS-$BC_{0.5}$/β-$CD_{0.5}$ composite: (a) pseudo-first order, (b) pseudo-second order, and (c) Elovich models.

surface of the Kaol/SLS-$BC_{0.5}$/β-$CD_{0.5}$. Additionally, increasing the processing temperature inside the *o*-NP–Kaol/SLS-$BC_{0.5}$/β-$CD_{0.5}$ system increases the *o*-NP kinetic energy, resulting in desorption of the *o*-NP molecules from the Kaol/SLS-$BC_{0.5}$/β-$CD_{0.5}$ surface.

3.2.5. Impact of the initial *o*-NP concentration. The influence of the *o*-NP concentration on the adsorption capability of the Kaol/SLS-$BC_{0.5}$/β-$CD_{0.5}$ composite was studied by varying the *o*-NP concentration between 50 and 300 mg L^{-1}. Fig. (4e) shows that the increase in the *o*-NP concentration resulted in an increase in the adsorption capability of Kaol/SLS-$BC_{0.5}$/β-$CD_{0.5}$ toward *o*-NP from 100 to 479.79 mg g^{-1}. Such an increase in the adsorption capacity of *o*-NP when its concentration was increased was due to the higher driving force from increased *o*-NP concentration, which overcomes mass transfer resistance and facilitates access to the Kaol/SLS-$BC_{0.5}$/β-$CD_{0.5}$ surface. Conversely, the removal percentage of *o*-NP was decreased from 100 to 69.43% upon increasing the *o*-NP concentration, as displayed in Fig. (S2), because of the minimal adsorption sites on the Kaol/SLS-$BC_{0.5}$/β-$CD_{0.5}$ surface compared to the amount of *o*-NP molecules.

3.3. Kinetic investigations

To scrutinize the nature of interactions between the *o*-NP molecules and the Kaol/SLS-$BC_{0.5}$/β-$CD_{0.5}$ composite, experimental data were analyzed using kinetic models, such as pseudo-first order, pseudo-second order, and Elovich, as demonstrated in Fig. (5a–c). The linear expressions of these kinetic models are shown in Table (S1). According to the derived parameters from the kinetic investigation shown in Table 2, the correlation coefficients of the *o*-NP adsorption curves for the pseudo-second-order model at various *o*-NP concentrations are almost equal to those of the pseudo-first order curves. However, the close agreement between the experimental equilibrium adsorption capacities of *o*-NP and the calculated values implies that the pseudo-second order model is favorable for describing *o*-NP adsorption onto Kaol/SLS-$BC_{0.5}$/β-$CD_{0.5}$. Consequently, the *o*-NP molecules adsorbed onto the active groups of the Kaol/SLS-$BC_{0.5}$/β-$CD_{0.5}$ surface with chemical interactions between them. Elovich analysis signaled that the desorption rate of *o*-NP is not as fast as the adsorption rate, confirming the favorability of *o*-NP adsorption onto Kaol/SLS-$BC_{0.5}$/β-$CD_{0.5}$.

3.4. Isotherm investigations

Analyzing the experimental equilibrium adsorption data using isotherm models is another way to identify whether the governing interaction is chemical or physical. Therefore, the *o*-NP adsorption data were assessed using linear expressions of the Langmuir, Freundlich, Temkin, and D–R models (Table S2). The correlation coefficient values of the isotherm curves (Fig. (6a–d)) of the *o*-NP adsorption onto Kaol/SLS-$BC_{0.5}$/β-$CD_{0.5}$ implied that physical interactions govern the adsorption reaction between *o*-NP and Kaol/SLS-$BC_{0.5}$/β-$CD_{0.5}$, where the adsorption data fit the Freundlich model. The Temkin model indicated the same finding as the Freundlich model, as *b* was less than 80 kJ mol^{-1} (Table 3), proving the dominance of the physical interactions in

Table 2 Pseudo-first order, pseudo-second order, and Elovich model parameters for the adsorption of *o*-NP onto Kaol/SLS-$BC_{0.5}$/β-$CD_{0.5}$

Kinetic models and parameters	Concentration (mg L^{-1})			
	50	100	200	300
$q_{e,\ Exp}$ (mg g^{-1})	93.02	168.04	327.94	443.81
Pseudo-first order				
$q_{e,\ Cal}$ (mg g^{-1})	85.23	134.29	155.99	292.16
k_1 (min^{-1})	0.047	0.045	0.044	0.043
R^2	0.997	0.995	0.991	0.992
Pseudo-second order				
$q_{e,\ Cal}$ (mg g^{-1})	111.11	196.07	357.14	500.00
k_2 (g mg^{-1} min^{-1})	5.8×10^{-4}	4.0×10^{-4}	3.7×10^{-4}	1.9×10^{-4}
R^2	0.998	0.999	0.999	0.999
Elovich				
α (mg g^{-1} min^{-1})	16.88	41.06	238.76	311.52
β (g mg^{-1})	4.3×10^{-2}	2.8×10^{-2}	2.2×10^{-2}	1.3×10^{-2}
R^2	0.961	0.972	0.978	0.984

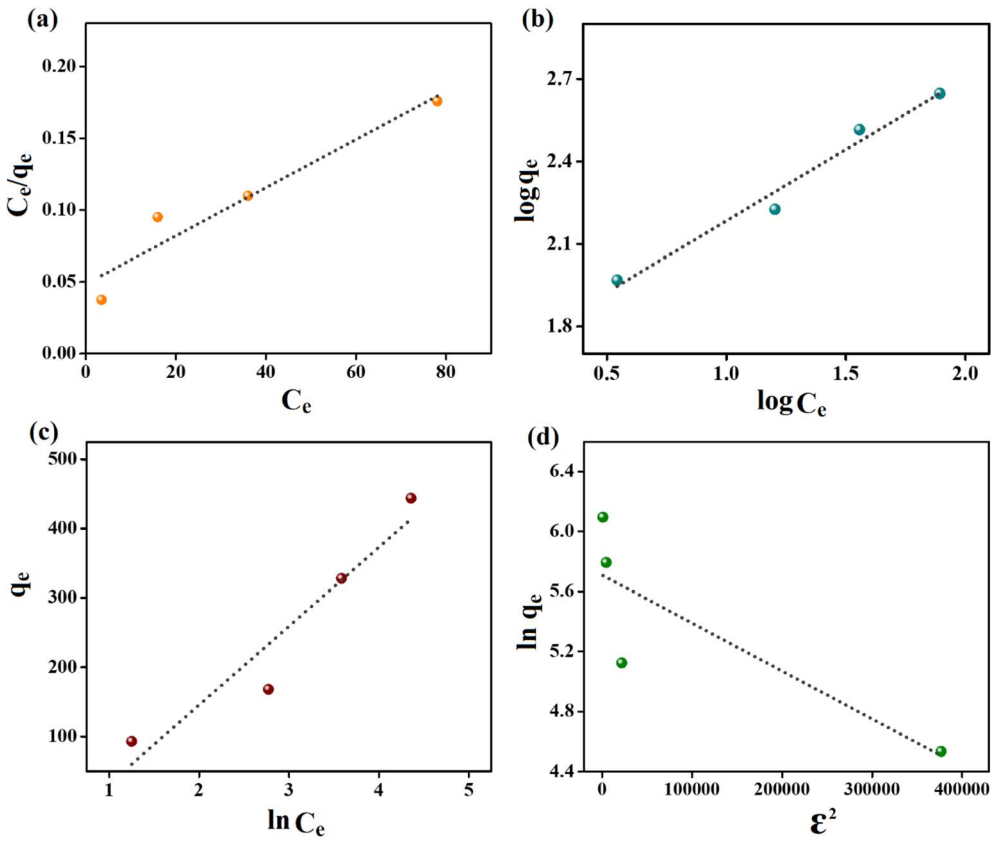

Fig. 6 Isotherm inspections of *o*-NP adsorption onto the Kaol/SLS-$BC_{0.5}$/β-$CD_{0.5}$ composite: (a) Langmuir, (b) Freundlich, (c) Temkin, and (d) D–R models.

adsorbing *o*-NP onto Kaol/SLS-$BC_{0.5}$/β-$CD_{0.5}$. Furthermore, the Freundlich model showed the surface favorability of Kaol/SLS-$BC_{0.5}$/β-$CD_{0.5}$ to adsorb *o*-NP as the Freundlich constant exceeded unity. The Langmuir model revealed that the maximum capacity of the Kaol/SLS-$BC_{0.5}$/β-$CD_{0.5}$ composite to adsorb *o*-NP was 588.24 mg g^{-1}. Notably, the low correlation coefficient of the D–R curve reflected its unsuitability to model the *o*-NP adsorption onto Kaol/SLS-$BC_{0.5}$/β-$CD_{0.5}$.

3.5. Mechanistic study of the *o*-NP adsorption

According to the findings from the kinetic and isotherm analysis, the *o*-NP adsorption onto Kaol/SLS-$BC_{0.5}$/β-$CD_{0.5}$ occurred

Table 3 Parameters of Langmuir, Freundlich, Temkin, and D–R isotherms for the adsorption of *o*-NP onto Kaol/SLS-$BC_{0.5}$/β-$CD_{0.5}$

Isotherm model	Parameters	Values
Langmuir	q_{max} (mg g^{-1})	588.24
	K_L (L mg^{-1})	0.0349
	R^2	0.929
Freundlich	n	1.93
	K_F ((mg g^{-1}) (L $mg^{-1})^{1/n}$)	46.16
	R^2	0.977
Temkin	k_T (L mg^{-1})	2.05
	b_T (KJ mol^{-1})	21.43
	R^2	0.917
D–R	q_s (mg g^{-1})	301.60
	K_{DR} (mol^2 J^{-2})	3.00×10^{-6}
	E (kJ mol^{-1})	0.408
	R^2	0.709

through different physical and chemical interactions between the composite and *o*-NP. Notably, in the XPS wide spectrum, the appearance of the peak corresponding to nitrogen of the used Kaol/SLS-$BC_{0.5}$/β-$CD_{0.5}$ (Fig. (7a)) confirms the adsorption of *o*-NP onto the composite. Moreover, the generation of interactions between Kaol/SLS-$BC_{0.5}$/β-$CD_{0.5}$ and *o*-NP was suggested by the interpretation of the changes in the XPS spectra of the composite after the adsorption reaction as follows:

π–π interaction is a suggested pathway for the adsorption of *o*-NP onto Kaol/SLS-$BC_{0.5}$/β-$CD_{0.5}$, as both contain aromatic rings. Consequently, the phenolic ring of *o*-NP could interact with the benzene ring of biochar in the Kaol/SLS-$BC_{0.5}$/β-$CD_{0.5}$ composite. The change in the position of the C1s peak of Kaol/SLS-$BC_{0.5}$/β-$CD_{0.5}$ after adsorbing the *o*-NP molecules (Fig. (7b)) reflected the bonding of *o*-NP and the composite by π–π

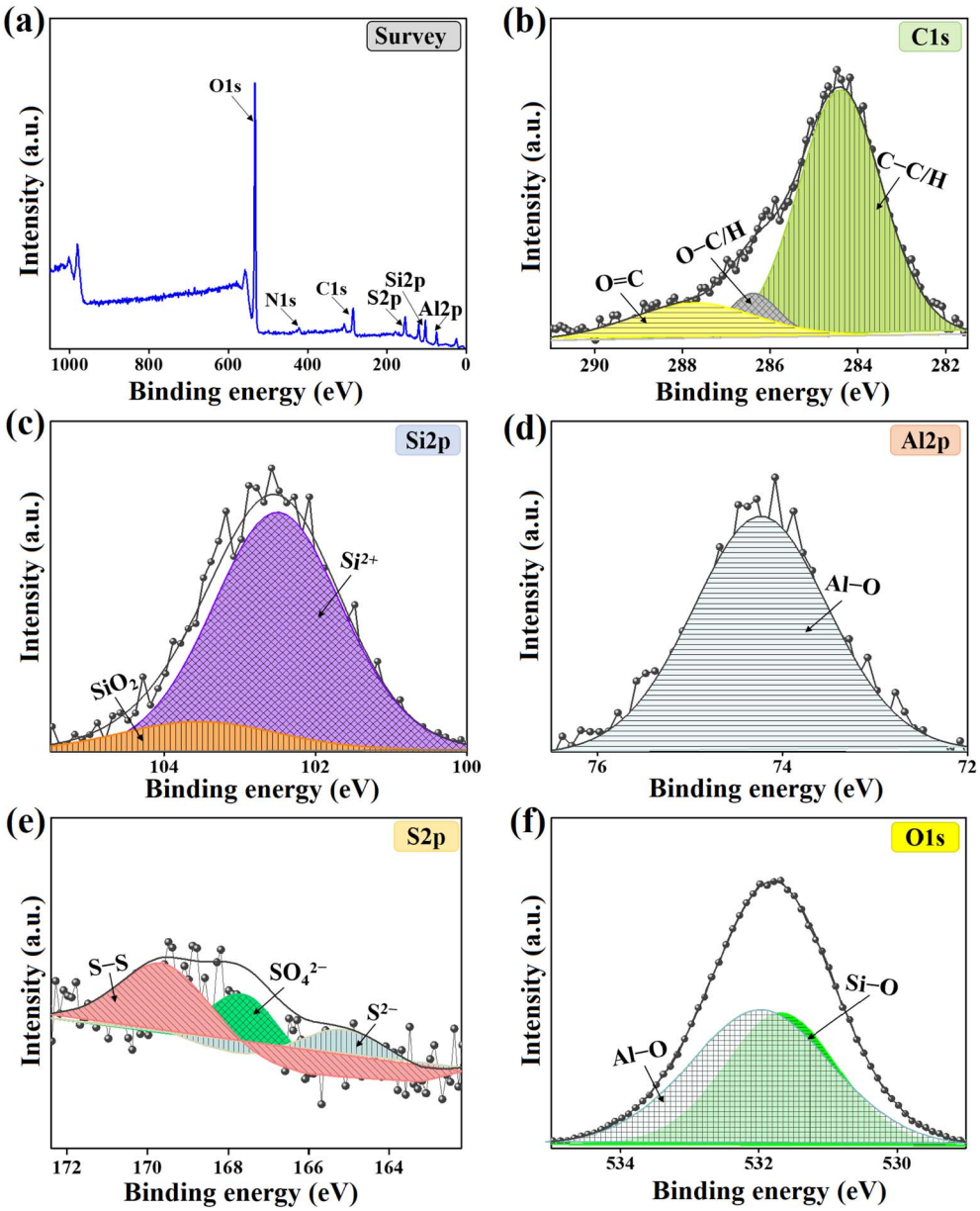

Fig. 7 XPS spectra of the used Kaol/SLS-$BC_{0.5}$/β-$CD_{0.5}$ composite: (a) XPS survey, (b) C1s, (c) Si2p, (d) Al2p, (e) S2p, and (f) O1s.

Table 4 BBD design of process variables for experiments and values of experimental data for *o*-NP adsorption onto Kaol/SLS-BC/β-CD

					R%	
Std	Run	*A*: conc. (mg L^{-1})	*B*: dose (mg)	*C*: time (min)	Experimental	Predicted
4	1	300	15	61	64.61	65.32
11	2	175	5	120	52.44	59.77
13	3	175	10	61	69.44	65.75
15	4	175	10	61	69.44	65.75
7	5	50	10	120	100	89.27
2	6	300	5	61	26.38	36.25
14	7	175	10	61	69.44	65.75
8	8	300	10	120	64.24	59.35
3	9	50	15	61	99.78	95.24
1	10	50	5	61	60.94	66.17
9	11	175	5	2	7.33	−2.89
5	12	50	10	2	17.72	26.61
12	13	175	15	120	80.56	88.84
6	14	300	10	2	3.33	−3.31
10	15	175	15	2	18.21	26.18

interaction. In addition, the coordination bond takes part in adsorbing *o*-NP onto Kaol/SLS-$BC_{0.5}$/β-$CD_{0.5}$ as *o*-NP comprises hydroxyl species that can create a coordination bond with aluminum and silicon of the kaolin in the composite structure. Fig. (7c and d) show a shift of the peaks of the Si2p and Al2p spectra for the used Kaol/SLS-$BC_{0.5}$/β-$CD_{0.5}$, reflecting their contribution to the adsorption reaction of *o*-NP.

The Lewis acid–base interaction is a governing adsorption mechanism in the adsorption process of *o*-NP onto Kaol/SLS-$BC_{0.5}$/β-$CD_{0.5}$, in which *o*-NP contains a Lewis acid (nitro group) and a Lewis base (hydroxyl group). Meanwhile, Kaol/SLS-$BC_{0.5}$/β-$CD_{0.5}$ possesses sulfate and hydroxyl groups that act as Lewis bases; in addition, aluminum and silicon act as Lewis acids. Therefore, the Lewis acid and base species of both *o*-NP and Kaol/SLS-$BC_{0.5}$/β-$CD_{0.5}$ could interact *via* Lewis acid–base interactions. The sulfur and oxygen spectra of the Kaol/SLS-$BC_{0.5}$/β-$CD_{0.5}$ after *o*-NP adsorption revealed shifts in their characteristic peaks, as shown in Fig. (7e and f), suggesting the involvement of sulfur and oxygen in the adsorption process.

Hydrogen bonds can be proposed as an influence adsorption pathway during the removal of *o*-NP by Kaol/SLS-$BC_{0.5}$/β-$CD_{0.5}$ as the *o*-NP molecules comprise NO_2 (H-acceptor) and OH (H-donor), while OH and COOH of Kaol/SLS-$BC_{0.5}$/β-$CD_{0.5}$ act as both H-donor and H-acceptor. Consequently, a hydrogen bond could be formed between NO_2 of *o*-NP (H-acceptor) and OH and COOH of Kaol/SLS-$BC_{0.5}$/β-$CD_{0.5}$ (H-donor). In parallel, OH of *o*-NP acts as an H-donor to attach with OH and COOH of Kaol/SLS-$BC_{0.5}$/β-$CD_{0.5}$ (H-acceptor) *via* a hydrogen bond. The *o*-NP dimensions are 6.87 × 14.38 × 6.43 Å, and the cavity size of β-CD is around 0.6–0.65 nm, as the NO_2 of *o*-NP is located within the β-CD cavity, and the OH of *o*-NP can interact with the secondary OH groups of the β-CD.[49,50] Therefore, pore-filling can be a significant adsorption pathway in the *o*-NP adsorption reaction, where β-CD of Kaol/SLS-$BC_{0.5}$/β-$CD_{0.5}$ has a wide cavity that expands to adsorb *o*-NP inside it.

Unexpectedly, electrostatic interactions do not domination in the adsorptive removal of *o*-NP by Kaol/SLS-$BC_{0.5}$/β-$CD_{0.5}$ as *o*-NP exists predominantly in its molecular form below pH 7.23. In contrast, increasing the pH over 7.23 results in the conversion of

Table 5 ANOVA for the response surface quadratic polynomial model for *o*-NP adsorption onto Kaol/SLS-BC/β-CD[a]

Source	Sum of squares	df	Mean square	*F*-value	*p*-value	
Model	13 618.34	9	1513.15	19.42	0.0022	Significant
A – conc.	1790.41	1	1790.41	22.98	0.0049	
B – dose	1689.84	1	1689.84	21.69	0.0055	
C – time	7853.18	1	7853.18	100.78	0.0002	
AB	0.0420	1	0.0420	0.0005	0.9824	
AC	114.17	1	114.17	1.47	0.2802	
BC	74.30	1	74.30	0.9536	0.3737	
A^2	0.0467	1	0.0467	0.0006	0.9814	
B^2	159.62	1	159.62	2.05	0.2118	
C^2	1992.49	1	1992.49	25.57	0.0039	
Residual	389.60	5	77.92			
Lack of fit	389.60	3	129.87			
Pure error	0.0000	2	0.0000			
Cor total	14 007.95	14				

[a] Std deviation: 8.83; mean: 53.60; coefficient of variation %: 16.47; R^2: 0.9722; adjusted R^2: 0.9221; predicted R^2: 0.5550; adequate precision: 13.857.

Table 6 ANOVA for the reduced quadratic model[a]

Source	Sum of squares	df	Mean square	*F*-value	*p*-value	
Model	13 264.11	4	3316.03	44.85	<0.0001	Significant
A – conc.	1796.40	1	1796.40	24.30	0.0006	
B – dose	1684.03	1	1684.03	22.78	0.0008	
C – time	7853.18	1	7853.18	106.21	<0.0001	
C^2	1930.50	1	1930.50	26.11	0.0005	
Residual	739.39	10	73.94			
Lack of fit	739.39	8	92.42			
Pure error	0.0000	2	0.0000			
Cor total	14 003.50	14				

[a] Std deviation: 8.60; mean: 53.59; coefficient of variation %: 16.05; R^2: 0.9472; adjusted R^2: 0.9261; predicted R^2: 0.8668; adequate precision: 19.8509.

o-NP to anionic species. Therefore, electrostatic repulsion works to decrease the adsorption efficiency of *o*-NP onto Kaol/SLS-$BC_{0.5}$/β-$CD_{0.5}$ in neutral and alkaline media. The experimental results from studying the influence of changing the pH on the efficacy of the *o*-NP adsorption confirmed the negative role of electrostatic repulsion in decreasing the removal ability of *o*-NP.

3.6. Statistical optimization of the adsorption of *o*-NP

The BBD for *o*-NP adsorption onto Kaol/SLS-BC/β-CD, along with experimental and predicted responses, is summarized in Table 4. To identify the most suitable regression model, analysis of variance (ANOVA) was performed for linear and quadratic equations. Of these, the quadratic model provided the best fit,

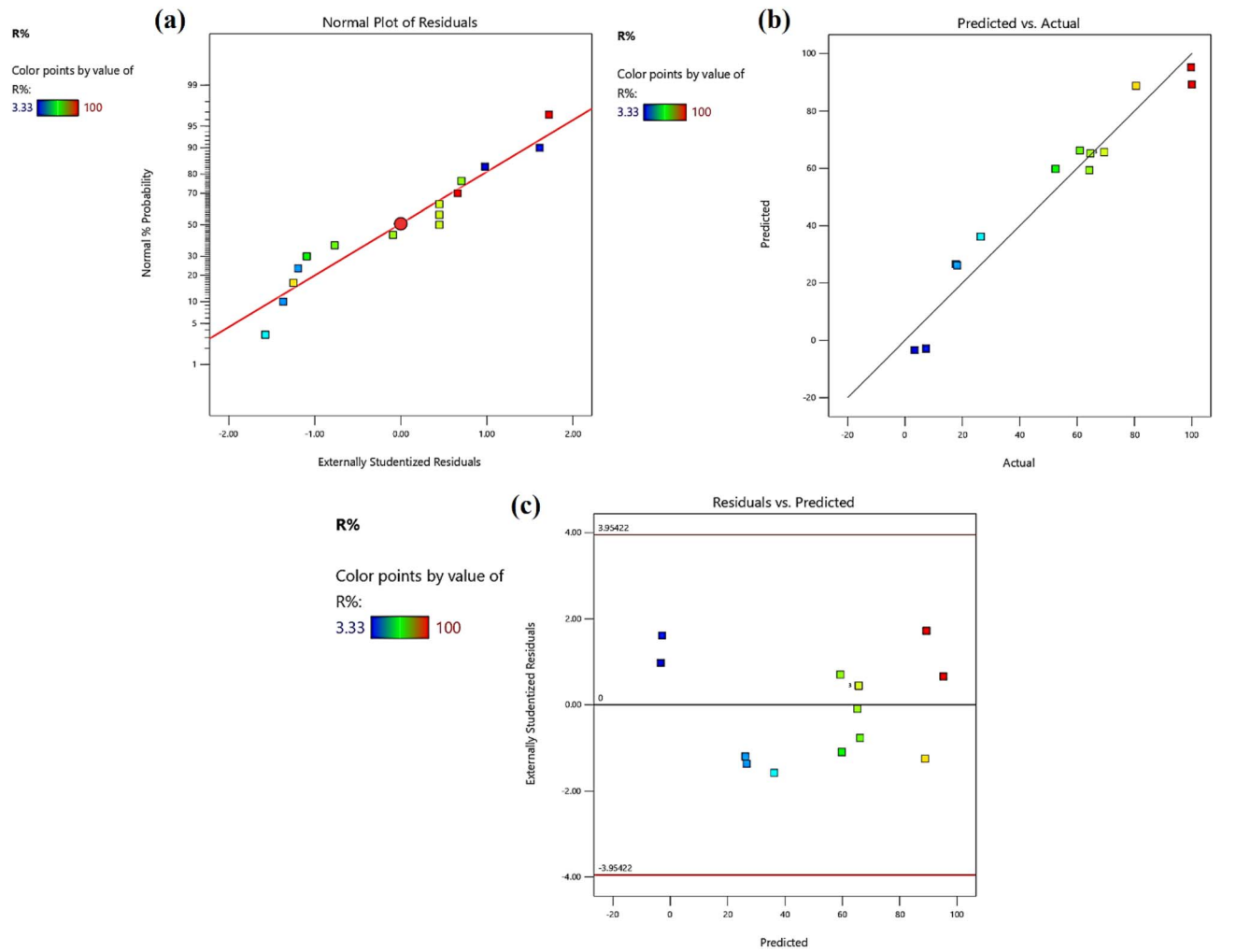

Fig. 8 (a) Normal probability plot of residuals for *o*-NP removal, (b) plot of experimental *versus* predicted values, and (c) plot of residuals against experimental values.

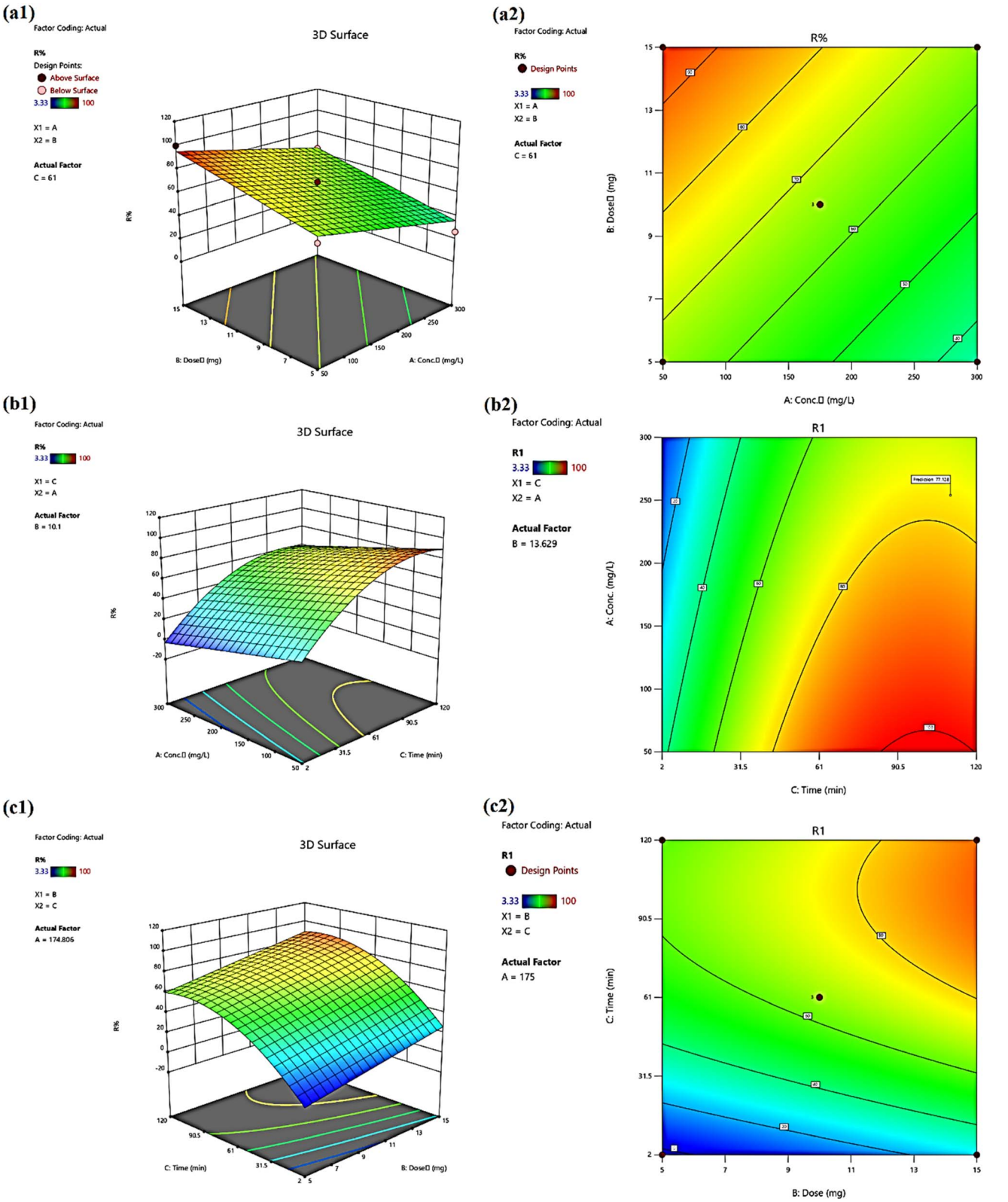

Fig. 9 Three-dimensional surface plots and contour plots of (a1 and a2) initial *o*-NP concentration and adsorbent dosage, (b1 and b2) initial *o*-NP concentration and contact time, and (c1 and c2) adsorbent dosage and contact time.

yielding high R^2 and adjusted R^2 values, and was therefore selected for further analysis.

The quadratic response surface model was evaluated using ANOVA. As shown in Table 5, the model *F*-value of 19.42 confirmed the overall significance, although several terms were statistically insignificant. The adjusted R^2 value was 0.922, while the predicted R^2 was 0.555, and the difference between the adjusted and predicted R^2 exceeded the acceptable threshold of 0.2, indicating possible block effects or issues with the model or data. In addition, *p*-values less than 0.0500 indicate model terms are significant. In this case *A*, *B*, *C*, and C^2 are significant model terms. Values greater than 0.100 indicate that the model terms are not significant.

To improve the model, non-significant terms were sequentially removed using a stepwise reduction approach. The refined model retained only significant variables, resulting in improved R^2, adjusted R^2, and predicted R^2 values. The final ANOVA results are summarized in Table 6, and the reduced regression equation for *o*-NP adsorption is presented as eqn (4):

$$R\% = +65.72 - 14.99A + 14.51B + 31.33C - 22.74C^2 \quad (4)$$

where *R*% represents the *o*-NP removal efficiency, *A* denotes the initial *o*-NP concentration, *B* the adsorbent dose, and *C* the contact time.

As shown in Table 6, the model exhibited an *F*-value of 44.85, confirming its statistical significance, with <0.0001% probability that such a value could arise from random noise.

The predicted R^2 reflects the model's ability to estimate response values. For a model to be considered adequate, the difference between the adjusted R^2 and predicted R^2 should fall within 0–0.20. In this case, the predicted R^2 (0.867) was in a good agreement with the adjusted R^2 (0.926). Adequate precision, which measures the signal-to-noise ratio, was 19.851, exceeding the desirable threshold of 4. These results confirm that the model provides an adequate signal and can be reliably used to explore the design space.

Fig. (8a) presents the normal probability plot of residuals for *o*-NP removal, illustrating the degree to which the observed values followed the theoretical distribution. As shown in Fig. (8b), the experimental data points were closely aligned, indicating approximate normality. This confirms that the regression model reliably describes the data, accounting for about 92.61% of the response variability. Furthermore, the residual analysis (Fig. (8c)) revealed a random scatter without any distinct pattern, further supporting the adequacy of the model.

Design-Expert software was used to generate fitted response surface plots in order to visualize the interactions among the key parameters influencing the optimal adsorption of *o*-NP. These plots are presented in Fig. (9). As shown in Fig. (9a1 and a2), the response surfaces depict the relationship between the initial *o*-NP concentration and the adsorbent dosage in the adsorption process onto Kaol/SLS-BC/β-CD. Increasing the adsorbent dosage improved the *o*-NP adsorption efficiency ratios on Kaol/SLS-BC/β-CD due to the availability of sites on Kaol/SLS-BC/β-CD as the dosage increased. In addition, an increase in the adsorption efficiency ratio was observed (from 26.38% to 99.78%) with decreasing initial *o*-NP concentration (from 300 to 50 mg L^{-1}). This is because at low adsorbent concentrations, there are sufficient active sites on the adsorbent, and there is no competition among adsorbed molecules.

Fig. (9b1 and b2) illustrate the interaction between treatment time and initial *o*-NP concentration in relation to adsorption efficiency. The results clearly demonstrate the pronounced influence of contact time on the adsorption process. A maximum removal efficiency was obtained at lower initial concentrations of *o*-NP, whereas raising the concedntrations decreased the removal capacity gradually. Prolonged contact time increased the adsorption capacity of Kaol/SLS-BC/β-CD toward *o*-NP. Fig. (9c1 and c2) illustrate the interaction between adsorbent dosage and contact time with respect to adsorption efficiency. The results highlight the significant effect of contact time on the adsorption process. It is also observed that the adsorption efficiency increases with increasing adsorbent dosage.

3.7. Cycling test

As recyclability is a significant trait in excellent adsorbents, cycling testing of Kaol/SLS-$BC_{0.5}$/β-$CD_{0.5}$ was carried out for six adsorption runs of *o*-NP, as illustrated in Fig. 10. Clearly, the removal efficacy of Kaol/SLS-$BC_{0.5}$/β-$CD_{0.5}$ towards *o*-NP decreased, with a slightly lower value that was not decreased by more than 3.00% in the first three adsorption runs. In addition, the overall decrease in the removal % of *o*-NP was about 8.96% during the six runs. Furthermore, the elemental compositions of the pure and recyclable Kaol/SLS-$BC_{0.5}$/β-$CD_{0.5}$ composite were determined by XPS analysis (Table S3). No considerable decrease was observed in the atomic % of silicon, aluminum, carbon, and sulfur of Kaol/SLS-$BC_{0.5}$/β-$CD_{0.5}$ composite after the *o*-NP adsorption reaction. In addition, the atomic % of oxygen slightly increased with the appearance of nitrogen atoms. These findings suggest that the slight decrease in the adsorption capacity of Kaol/SLS-$BC_{0.5}$/β-$CD_{0.5}$ after each cycle could be attributed to strong interactions between *o*-NP and the

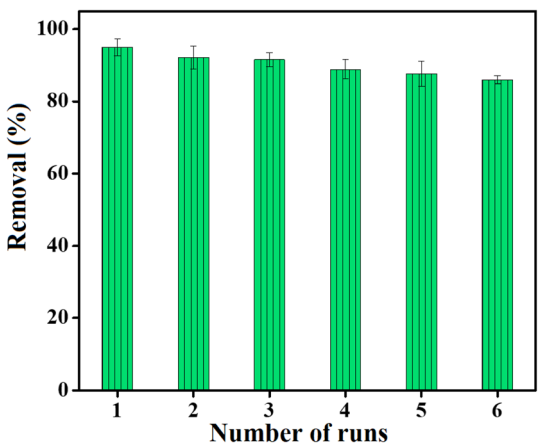

Fig. 10 Results of the recycling test of the Kaol/SLS-$BC_{0.5}$/β-$CD_{0.5}$ composite for the adsorption of *o*-NP.

Table 7 A comparison between the adsorption abilities of the Kaol/SLS-$BC_{0.5}$/β-$CD_{0.5}$ composite and previously reported adsorbents toward *o*-NP

Adsorbent	q_{max} (mg g^{-1})	Eq. time (min)	Reference
Fe_3O_4/AP-coke/N-Cs	291.55	100	5
ACWC activated carbon	179.10	300	51
Fe_3O_4-κ-Carr/MIL-125(Ti)	320.26	60	52
WH activated carbon	47.62	180	53
SM CLI–PPHF	1.51	1080	54
Nano zeolite	143.80	150	55
Kaol/SLS-$BC_{0.5}$/β-$CD_{0.5}$	588.24	90	This study

composite, which result in some of the *o*-NP remaining strongly bound to active sites and the internal pores of the composite even after the regeneration step. In addition, there is the possibility of the loss of some Kaol/SLS-$BC_{0.5}$/β-$CD_{0.5}$ during the recovery stage after the adsorption runs. More importantly, the cycling test confirmed the chemical stability of Kaol/SLS-$BC_{0.5}$/β-$CD_{0.5}$, which was durable for many adsorption cycles.

3.8. Comparison study

Although the presence of residual *o*-NP from industrial sources poses a serious threat, there is a lack of comprehensive studies addressing its removal by adsorption or catalysis. Meanwhile, there are no investigations involving the adsorption of *o*-NP onto Kaol, SLS-BC, or β-CD. The adsorption performance of the novel Kaol/SLS-$BC_{0.5}$/β-$CD_{0.5}$ composite was compared with the reported adsorbents in previous assessments, as shown in Table 7. The comparison table reveals the promising adsorption capacity of Kaol/SLS-$BC_{0.5}$/β-$CD_{0.5}$ toward *o*-NP, as it provides a higher adsorption capacity compared to other adsorbents in a short equilibrium time. Such superiority of the Kaol/SLS-$BC_{0.5}$/β-$CD_{0.5}$ could be attributed to the remarkable composition of the composite. Kaol provides silicon and aluminum atoms, which can bond to *o*-NP *via* coordination bonds and Lewis acid–base interactions. Moreover, SLS-BC contains aromatic rings, and sulfate and hydroxyl groups; consequently, it can adsorb *o*-NP *via* Lewis acid–base interactions, pi–pi interactions, and hydrogen bonds. The loose cavity of β-CD enables it to host *o*-NP molecules, and the NO_2 group enters the cavity, and the OH of *o*-NP can interact with the secondary OH of β-CD.[50] Additionally, the abundant hydroxyl groups on the β-CD structure facilitate its interaction with *o*-NP by Lewis acid–base interaction.

4. Conclusion

In this work, a novel adsorbent was synthesized for the first time using Kaol, SLS-BC, and β-CD, which have not previously been applied for *o*-NP adsorption. The Kaol/SLS-$BC_{0.5}$/β-$CD_{0.5}$ composite was engineered and well-analyzed using a number of characterization techniques such as XRD, ZP, SEM, XPS, and FTIR. The FTIR and SEM of Kaol/SLS-$BC_{0.5}$/β-$CD_{0.5}$ confirmed the good combination of the pure Kaol, SLS-BC, and β-CD in the composite matrix. In addition, the ZP analysis of Kaol/SLS-$BC_{0.5}$/β-$CD_{0.5}$ implied that it has no charge at pH = 5.88. The results from the batch experiments of the adsorption of *o*-NP onto Kaol/SLS-$BC_{0.5}$/β-$CD_{0.5}$ showed that a more acidic adsorption medium and room temperature are the best conditions to set up the *o*-NP–Kaol/SLS-$BC_{0.5}$/β-$CD_{0.5}$ system. The data analysis using isotherm and kinetic models clarified the favorability of the Freundlich and pseudo-second-order models to model the *o*-NP adsorption reaction. Adsorption pathways of *o*-NP to attach the active groups onto Kaol/SLS-$BC_{0.5}$/β-$CD_{0.5}$ were proposed in light of the XPS patterns of pure and used Kaol/SLS-$BC_{0.5}$/β-$CD_{0.5}$. Finally, Kaol/SLS-$BC_{0.5}$/β-$CD_{0.5}$ revealed promising recycling ability; however, we recommend adding a magnetic substance to the composite or encapsulating it inside a polymeric bead or membrane to avoid losing part of it during the recovery. The adsorption of *o*-NP onto Kaol/SLS-$BC_{0.5}$/β-$CD_{0.5}$ was modeled using RSM based on a BBD. The experimental design, regression analysis, and quadratic models developed through RSM were found to be accurate and effective in predicting the adsorption efficiency within the studied factor ranges. The reduced quadratic model demonstrated good agreement between predicted and experimental values, with the contact time identified as a key parameter influencing the response. Overall, RSM proved to be a powerful tool for optimizing *o*-NP adsorption onto Kaol/SLS-$BC_{0.5}$/β-$CD_{0.5}$, enabling reduced experimental effort, shorter research duration, and lower costs.

Conflicts of interest

The authors declare no competing interests.

Data availability

The datasets supporting the findings of this study are available within the article and its supplementary information (SI) files. Supplementary information is available. See DOI: https://doi.org/10.1039/d5ra08005c.

Acknowledgements

The Researchers would like to thank the Deanship of Graduate Studies and Scientific Research at Qassim University for financial support (QU-APC-2025).

References

1 W. S. Koe, *et al.*, An overview of photocatalytic degradation: photocatalysts, mechanisms, and development of photocatalytic membrane, *Environ. Sci. Pollut. Res.*, 2020, **27**(3), 2522–2565.
2 E. Zhang, *et al.*, A novel amino functionalized three-dimensional fluorescent Zn-MOF: The synthesis, structure and applications in the fluorescent sensing of organic water pollutants, *J. Mol. Struct.*, 2022, **1264**, 133314.
3 S. Zhu, *et al.*, Enhanced removal of Ni2+ and Co2+ from wastewater using a novel 2-hydroxyphosphonoacetic acid

modified Mg/Fe-LDH composite adsorbent, *Water Res.*, 2025, **272**, 122997.
4 B. S. Marques, *et al.*, Ca–Al, Ni–Al and Zn–Al LDH powders as efficient materials to treat synthetic effluents containing o-nitrophenol, *J. Alloys Compd.*, 2020, **838**, 155628.
5 A. M. Omer, *et al.*, Sustainable synthesis of magnetic petroleum coke/nonanyl chitosan composite for efficient removal of o-nitrophenol, *Sci. Rep.*, 2024, **14**(1), 14463.
6 D. Ewis, *et al.*, Adsorption of 4-nitrophenol onto iron oxide bentonite nanocomposite: process optimization, kinetics, isotherms and mechanism, *Int. J. Environ. Res.*, 2022, **16**(2), 23.
7 M. Kuddushi, *et al.*, A transparent, tough and self-healable biopolymeric composites hydrogel for open wound management, *ACS Appl. Bio Mater.*, 2023, **6**(9), 3810–3822.
8 D. Khan, J. Kuntail and I. Sinha, Mechanism of phenol and p-nitrophenol adsorption on kaolinite surface in aqueous medium: A molecular dynamics study, *J. Mol. Graph. Model.*, 2022, **116**, 108251.
9 Y. Yang, *et al.*, Bicarbonate-enhanced iron-based Prussian blue analogs catalyze the Fenton-like degradation of p-nitrophenol, *J. Colloid Interface Sci.*, 2022, **608**, 2884–2895.
10 S. Barakan and V. Aghazadeh, The advantages of clay mineral modification methods for enhancing adsorption efficiency in wastewater treatment: a review, *Environ. Sci. Pollut. Res.*, 2021, **28**(3), 2572–2599.
11 L. Mouni, *et al.*, Removal of Methylene Blue from aqueous solutions by adsorption on Kaolin: Kinetic and equilibrium studies, *Appl. Clay Sci.*, 2018, **153**, 38–45.
12 J. Hizal and R. Apak, Modeling of cadmium (II) adsorption on kaolinite-based clays in the absence and presence of humic acid, *Appl. Clay Sci.*, 2006, **32**(3–4), 232–244.
13 K. G. Bhattacharyya and S. S. Gupta, Adsorption of a few heavy metals on natural and modified kaolinite and montmorillonite: a review, *Adv. Colloid Interface Sci.*, 2008, **140**(2), 114–131.
14 R. Duarte-Silva, *et al.*, Structural, textural and protein adsorption properties of kaolinite and surface modified kaolinite adsorbents, *Appl. Clay Sci.*, 2014, **90**, 73–80.
15 W. Gao, *et al.*, Direct acid activation of kaolinite and its effects on the adsorption of methylene blue, *Appl. Clay Sci.*, 2016, **126**, 98–106.
16 S. M. Shaheen, *et al.*, Wood-based biochar for the removal of potentially toxic elements in water and wastewater: a critical review, *Int. Mater. Rev.*, 2019, **64**(4), 216–247.
17 J. Maroušek, *et al.*, Modified biochars present an economic challenge to phosphate management in wastewater treatment plants, *J. Clean. Prod.*, 2020, **272**, 123015.
18 G. Prasannamedha, *et al.*, Enhanced adsorptive removal of sulfamethoxazole from water using biochar derived from hydrothermal carbonization of sugarcane bagasse, *J. Hazard. Mater.*, 2021, **407**, 124825.
19 R. Deng, *et al.*, Biochar-mediated Fenton-like reaction for the degradation of sulfamethazine: Role of environmentally persistent free radicals, *Chemosphere*, 2020, **255**, 126975.
20 J. Y. Liu, X. Zhang and B. TIAN, Selective modifications at the different positions of cyclodextrins: a review of strategies, *Turk. J. Chem.*, 2020, **44**(2), 261–278.
21 S. V. Kurkov and T. Loftsson, Cyclodextrins, *Int. J. Pharm.*, 2013, **453**(1), 167–180.
22 L. Ding, *et al.*, Studies on a novel modified β-cyclodextrin inclusion complex, *J. Mol. Struct.*, 2010, **979**(1–3), 122–127.
23 J. Wankar, *et al.*, Recent advances in host–guest self-assembled cyclodextrin carriers: Implications for responsive drug delivery and biomedical engineering, *Adv. Funct. Mater.*, 2020, **30**(44), 1909049.
24 R. Q. Wang, X. B. Wei and Y. Q. Feng, β-Cyclodextrin covalent organic framework for selective molecular adsorption, *Chem.–Eur. J.*, 2018, **24**(43), 10979–10983.
25 B. Tian, Y. Liu and J. Liu, Smart stimuli-responsive drug delivery systems based on cyclodextrin: A review, *Carbohydr. Polym.*, 2021, **251**, 116871.
26 S. Jacob and A. B. Nair, Cyclodextrin complexes: Perspective from drug delivery and formulation, *Drug Dev. Res.*, 2018, **79**(5), 201–217.
27 T. Rajkumar, *et al.*, Cyclodextrin-metal–organic framework (CD-MOF): From synthesis to applications, *J. Ind. Eng. Chem.*, 2019, **72**, 50–66.
28 Y. Liu, *et al.*, β-Cyclodextrin-based hollow nanoparticles with excellent adsorption performance towards organic and inorganic pollutants, *Nanoscale*, 2019, **11**(40), 18653–18661.
29 M. Fu, *et al.*, Adsorption performance and mechanism of pectin modified with β-cyclodextrin for Zn2+ and Cu2+, *Int. J. Biol. Macromol.*, 2024, **274**, 133563.
30 J. Rajewski and A. Dobrzyńska-Inger, Application of response surface methodology (RSM) for the optimization of chromium (III) synergistic extraction by supported liquid membrane, *Membranes*, 2021, **11**(11), 854.
31 J. Rajewski, P. Religa and P. Gierycz, The possibility of using a mathematical model based on consecutive first-order reactions to describe the Cr (III) ions pertraction in DCSLM system, *Res. Chem. Intermed.*, 2017, **43**(10), 5569–5585.
32 S. S. Gabr, *et al.*, RSM-CCD optimized adsorptive removal of p-Nitrophenol using Eco-Friendly magnetic activated carbon thin Film, *Inorg. Chem. Commun.*, 2025, **178**, 114471.
33 H. Qu, S. He and H. Su, Efficient preparation of kaolinite/methanol intercalation composite by using a Soxhlet extractor, *Sci. Rep.*, 2019, **9**(1), 8351.
34 B. Meroufel and M. A. Zenasni, Preparation, characterization, and heavy metal ion adsorption property of APTES-modified kaolin: comparative study with original clay, in *Handbook of Environmental Materials Management*, Springer, 2019, pp. 1167–1190.
35 N. Belachew and H. Hinsene, Preparation of zeolite 4A for adsorptive removal of methylene blue: optimization, kinetics, isotherm, and mechanism study, *Silicon*, 2022, **14**(4), 1629–1641.
36 E. Behazin, *et al.*, Mechanical, chemical, and physical properties of wood and perennial grass biochars for possible composite application, *BioResources*, 2016, **11**(1), 1334–1348.

37 S. H. M. Jessima, A. Berisha and S. S. Srikandan, Preparation, characterization, and evaluation of corrosion inhibition efficiency of sodium lauryl sulfate modified chitosan for mild steel in the acid pickling process, *J. Mol. Liq.*, 2020, **320**, 114382.
38 B. Meroufel, *et al.*, Removal of Zn (II) from aqueous solution onto kaolin by batch design, *J. Water Resour. Protect.*, 2013, **5**(07), 669.
39 M. Burachevskaya, *et al.*, Fabrication of biochar derived from different types of feedstocks as an efficient adsorbent for soil heavy metal removal, *Sci. Rep.*, 2023, **13**(1), 2020.
40 S. Muthuvijayan, *et al.*, Sodium lauryl sulphate-mediated synthesis: Unravelling the optimization path for enhanced stability and optical properties of cadmium sulphide nanoparticles, *Process Biochem.*, 2024, **138**, 57–66.
41 W. Song, *et al.*, Cyclodextrin-erythromycin complexes as a drug delivery device for orthopedic application, *Int. J. Nanomed.*, 2011, 3173–3186.
42 H. Sadaquat and M. Akhtar, Comparative effects of β-cyclodextrin, HP-β-cyclodextrin and SBE 7-β-cyclodextrin on the solubility and dissolution of docetaxel *via* inclusion complexation, *J. Inclusion Phenom. Macrocyclic Chem.*, 2020, **96**, 333–351.
43 J. Hao, *et al.*, Natural-Product-Tailored Polyurethane: Size-Dictated Construction of Polypseudorotaxanes with Cyclodextrin–Triterpenoid Pairs, *ACS Macro Lett.*, 2018, **7**(9), 1131–1137.
44 H. S. Nishad, *et al.*, Exchanging interlayer anions in NiFe-LDHs nanosphere enables superior battery-type storage for high-rate aqueous hybrid supercapacitors, *J. Mater. Chem. A*, 2024, **12**(16), 9494–9507.
45 N. Mahmud and A. Benamor, Magnetic iron oxide kaolinite nanocomposite for effective removal of congo red dye: adsorption, kinetics, and thermodynamics studies, *Water Conserv. Sci. Eng.*, 2023, **8**(1), 35.
46 K. Rouibah, *et al.*, Exploring the efficiency of Algerian kaolinite clay in the adsorption of Cr (III) from aqueous solutions: experimental and computational insights, *Molecules*, 2024, **29**(9), 2135.
47 H. Ma, *et al.*, Adsorption and regeneration of leaf-based biochar for p-nitrophenol adsorption from aqueous solution, *RSC Adv.*, 2019, **9**(67), 39282–39293.
48 L. Liu, G. Deng and X. Shi, Adsorption characteristics and mechanism of p-nitrophenol by pine sawdust biochar samples produced at different pyrolysis temperatures, *Sci. Rep.*, 2020, **10**(1), 1–11.
49 F. Iwasaki and Y. Kawano, The crystal and molecular structure of o-nitrophenol, *Struct. Sci.*, 1978, **34**(4), 1286–1290.
50 G. Crini, Y. Lekchiri and M. Morcellet, Separation of structural isomers using cyclodextrin-polymers coated on silica beads, *Chromatographia*, 1995, **40**(5), 296–302.
51 L. Sellaoui, *et al.*, Adsorption of ketoprofen and 2-nitrophenol on activated carbon prepared from winery wastes: a combined experimental and theoretical study, *J. Mol. Liq.*, 2021, **333**, 115906.
52 E. M. Abd El-Monaem, *et al.*, Adsorption of nitrophenol onto a novel Fe3O4-κ-carrageenan/MIL-125 (Ti) composite: process optimization, isotherms, kinetics, and mechanism, *Environ. Sci. Pollut. Res.*, 2023, **30**(17), 49301–49313.
53 T. O. Isichei and F. E. Okieimen, Adsorption of 2-nitrophenol onto water hyacinth activated carbon-kinetics and equilibrium studies, *Environ. Pollut.*, 2014, **3**(4), 99.
54 M. M. Motsa, *et al.*, Adsorption of 2, 4, 6-trichlorophenol and ortho-nitrophenol from aqueous media using surfactant-modified clinoptilolite–polypropylene hollow fibre composites, *Water, Air, Soil Pollut.*, 2012, **223**(4), 1555–1569.
55 T.-H. Pham, B.-K. Lee and J. Kim, Improved adsorption properties of a nano zeolite adsorbent toward toxic nitrophenols, *Process Saf. Environ. Prot.*, 2016, **104**, 314–322.